atmosphere

MDPI

Article

Spatiotemporal Evolution and Influencing Factors of Air Pollutants in the Three Major Urban Agglomerations of the Yellow River Basin

Yanli Yin [1], Fan Zhang [1], Qifan Wu [1], Linan Sun [2], Yuanzheng Li [2], Peng Wang [1], Zilin Liu [1], Tian Cui [1], Zhaomeng Zhou [1], Runjing Hou [1], Mingyang Zhang [1], Jinping Liu [1] and Qingfeng Hu [1,*]

[1] College of Surveying and Geo-Informatics, North China University of Water Resources and Electric Power, Zhengzhou 450046, China; yinyanli@ncwu.edu.cn (Y.Y.); z20241151143@stu.ncwu.edu.cn (F.Z.); wuqifan@ncwu.edu.cn (Q.W.); z20211151045@stu.ncwu.edu.cn (P.W.); z20231151103@stu.ncwu.edu.cn (Z.L.); cuitian@stu.ncwu.edu.cn (T.C.); z20241151133@stu.ncwu.edu.cn (Z.Z.); z20241151131@stu.ncwu.edu.cn (R.H.); z20241151130@stu.ncwu.edu.cn (M.Z.); liujp@radi.ac.cn (J.L.)

[2] School of Urban and Rural Planning, Henan University of Economics and Law, Zhengzhou 450046, China; sln@hnp.edu.cn (L.S.); yz_li@huel.edu.cn (Y.L.)

* Correspondence: huqingfeng@ncwu.edu.cn

Abstract

Against the backdrop of the ongoing advancement of China's dual-carbon goals and the coordinated strategy for ecological protection and high-quality development in the Yellow River Basin (YRB), it is important to clarify the spatiotemporal dynamics of air pollution in the densely populated urban agglomerations of the mid–lower YRB. Using station-based daily observations from 2015 to 2024, this study examines six major air pollutants ($PM_{2.5}$, PM_{10}, CO, NO_2, O_3 and SO_2) across the Shandong Peninsula, Central Plains, and Guanzhong Plain urban agglomerations. Sen's slope estimator and the Mann–Kendall test are applied to quantify long-term trends, while partial correlation analysis and the GeoDetector model are used to diagnose pollutant co-variations and the drivers of spatial heterogeneity. Results indicate that while $PM_{2.5}$, PM_{10}, NO_2, SO_2, and CO concentrations significantly decreased, O_3 exhibited a statistically significant upward trend ($Z = 2.32$, $p = 0.02$), particularly with pronounced summer maxima. $PM_{2.5}$ shows clear seasonal variation, with elevated levels during winter and reduced levels during summer. Marked spatial contrasts are also observed: elevated particulate matter and CO are concentrated in the northern part of the Central Plains, while higher O_3 levels are more evident in coastal areas, particularly within the Shandong Peninsula urban agglomeration. In terms of inter-pollutant relationships, particulate matter and CO are positively associated with SO_2, whereas O_3 is negatively correlated with NO_2. GeoDetector results further suggest that air temperature, wind speed, and topography are the key factors associated with the spatial differentiation of pollutant levels; notably, the interaction between wind speed and temperature provides the greatest explanatory power, with effects that vary seasonally. These findings provide a scientific basis for region-specific air-pollution control and for advancing the co-benefits of carbon reduction and pollution mitigation in the YRB.

Keywords: spatiotemporal evolution characteristics; pollutant covariation; trend analysis; partial correlation coefficient; GeoDetector

Check for updates

Academic Editors: Kaihui Zhao, Jie Li and Jun Hu

Received: 20 January 2026
Revised: 16 February 2026
Accepted: 24 February 2026
Published: 26 February 2026

Copyright: © 2026 by the authors. Licensee MDPI, Basel, Switzerland. This article is an open access article distributed under the terms and conditions of the Creative Commons Attribution (CC BY) license.

1. Introduction

Air pollution is one of the primary global environmental challenges and has been widely proven to be closely associated with the occurrence of various respiratory, cardiovascular, and cerebrovascular diseases [1]. Since the Industrial Revolution, the issue of atmospheric pollution has spread globally alongside the processes of urbanization and industrialization. Developed nations were the first to experience several iconic pollution events, such as the photochemical smog in London, UK, and the photochemical pollution in Silicon Valley, USA [2,3]. Entering the 21st century, developing countries like India and Brazil have also frequently suffered from severe haze and ozone pollution episodes [4–6]. As the world's largest developing country, China has witnessed a series of regional heavy pollution events during its rapid industrialization and urbanization [7]. To address this severe situation, China has successively implemented a series of environmental governance policies. Since 2013, the country has built and refined the National Ambient Air Quality Monitoring Network. In 2015, $PM_{2.5}$ monitoring was fully promoted in cities at or above the prefecture level. By deploying air quality monitoring stations in the urban areas of each prefecture-level city, the Ministry of Ecology and Environment has significantly enhanced the monitoring capacity and spatiotemporal resolution of multiple pollutants [8–10].

Acquiring pollutant data is merely a prerequisite; more importantly, it is essential to conduct comprehensive analyses of long-term time-series data [11]. Currently, atmospheric pollutant monitoring primarily relies on three technical approaches: ground-based station observations [12], satellite remote sensing retrieval [13], and numerical simulation [14]. The national automated ambient air quality monitoring stations now substantially cover prefecture-level cities and above across China, providing hourly observational data for multiple pollutants. This enables the accurate analysis of daily, monthly, seasonal, and multi-year variation trends [15,16]. In time-series trend analysis based on station data, parametric methods such as linear regression, cumulative anomaly, and sliding *t*-tests are commonly employed to describe fluctuations in pollutant concentrations [17–19]. However, considering that atmospheric environmental data often do not follow a strict normal distribution and exhibit seasonal fluctuations, research utilizing non-parametric statistical methods—such as Sen's slope estimator and the Mann–Kendall (MK) trend test—has gradually become mainstream in recent years. Compared with linear regression, it is more suitable for pollutants such as $PM_{2.5}$ and O_3, which show strong seasonality and non-normal data distributions [20,21]. Kernel density estimation and the global Moran's I index can visually show the spatial distribution of pollutants such as $PM_{2.5}$ and O_3 across the three urban agglomerations. By introducing trend analysis, the ten-year change trends of pollutants such as $PM_{2.5}$ and O_3 in the three urban agglomerations can be obtained, and the cities with the fastest declining trends within the study area can be identified, so that targeted regulation can be carried out for key cities.

Regarding analyses of factors influencing air pollutants, geographically weighted regression (GWR) and geographically and temporally weighted regression (GTWR) introduce weighting schemes that vary with geographic location and time, allowing regression coefficients to change across space and time, thereby describing how the influence intensity of different driving factors varies among regions and periods [22–24]. GeoDetector is often used to quantify spatial stratified heterogeneity and to compare the explanatory power of candidate drivers for observed pollutant patterns [25,26]. Explanatory variables have also expanded from meteorological conditions alone to include socio-economic indicators, context-specific human activities and interventions (e.g., short-term emission changes during the Spring Festival), and abrupt events such as the COVID-19 pandemic. Looking ahead, global warming is expected to intensify heatwaves [27–29]. Compound heatwaves not only exacerbate O_3 pollution but also increase the risk of heart disease and other ailments for

populations experiencing concurrent heat and pollution exposure [30,31]. Accurately identifying heatwaves is a prerequisite for addressing crises caused by global warming [32,33] and represents one of the future directions for atmospheric pollution research.

In terms of research scales, the spatiotemporal distribution and evolution patterns of air pollution can be explored across national, regional, urban, and even station-level scales. Domestically, most studies have focused on key urban agglomerations with high population densities and intensive emissions [34,35]. Regarding the Yellow River Basin (YRB), research has progressively shifted from macro-level analyses of individual cities or the entire basin toward a focus on the urban agglomeration scale. Studies have confirmed that high-pollutant zones within the basin are concentrated in the Central Plains, Shandong Peninsula, and Guanzhong Plain urban agglomerations in the mid–lower reaches [36–38]. Furthermore, while concentrations of pollutants such as SO_2 and NO_2 have exhibited a significant downward trend following the implementation of the "Air Pollution Prevention and Control Action Plan," the seasonal prominence of O_3 pollution has emerged as a new governance challenge [39,40].

While existing studies have yielded fruitful results regarding the spatiotemporal evolution and driving mechanisms of multi-pollutants at the urban agglomeration scale, providing essential references for this study, several critical knowledge gaps remain. First, existing studies mainly focus on coastal urban agglomerations including Beijing–Tianjin–Hebei, Yangtze River Delta, and Pearl River Delta. Comparative analyses among urban agglomerations and policy-driven differences are insufficient, especially systematic research on the three major agglomerations in the mid–lower Yellow River Basin. Second, most works focus on $PM_{2.5}$ or a limited number of pollutants; however, research on the synergistic evolution, correlation structures, and compound pollution characteristics of all six criteria pollutants ($PM_{2.5}$, PM_{10}, NO_2, O_3, CO, and SO_2) remains insufficient. Third, this study innovatively combines partial correlation analysis and the GeoDetector to integrate linear and nonlinear methods, yielding more scientific results. This study reveals the spatiotemporal evolution patterns and influencing factors of six pollutants across the three major urban agglomerations, providing empirical support for designing differentiated pollution reduction strategies targeting $PM_{2.5}$- or O_3-dominated pollution regimes in different cities (from coastal to inland regions) and across different seasons.

2. Materials and Methods

2.1. Study Area

The three major urban agglomerations in the middle and lower reaches of the Yellow River Basin (YRB), namely the Shandong Peninsula Urban Agglomeration (SPUA), the Central Plains Urban Agglomeration (CPUA), and the Guanzhong Plain Urban Agglomeration (GZPUA), represent three different types of geographical environments from the coastal area to the inland plain, and have unique meteorological and topographic conditions related to pollutant accumulation, transport, and photochemical formation. SPUA covers all 16 prefecture-level cities in Shandong Province. The CPUA includes 29 cities. While the GZPUA is centered on Xi'an and includes 11 prefecture-level cities. The specific city names are shown in Figure 1.

The SPUA is characterized by a complex topographical system comprising low hills, fault basins, and coastal plains. Bordering the Yellow Sea and the Bohai Sea, it possesses a temperate marine climate, with an average annual temperature of 11–14 °C and annual precipitation of 650–850 mm. The region is marked by a high level of urbanization, high population density, and a solid foundation for both industrial and agricultural development. The CPUA is located in the transition zone from the warm temperate to the subtropical zone. The northern part is dominated by a temperate monsoon climate, while the southern

part exhibits subtropical monsoon climate characteristics, featuring distinct seasons and synchronous heat and rain. It is one of the primary grain-producing regions in China. The GPUA is located in the climatic transition zone between northern and southern China. The core area belongs to a temperate continental climate, with an annual mean temperature of about 6–13 °C and annual precipitation of about 500–900 mm. In terms of topography, it is bordered by the Qinling Mountains to the south and the Loess Plateau to the north, and the middle part is a lowland corridor formed by the Weihe alluvial plain. This topography is prone to pollutant accumulation under stable meteorological conditions, and it can also transport pollutants to other regions through monsoon circulation.

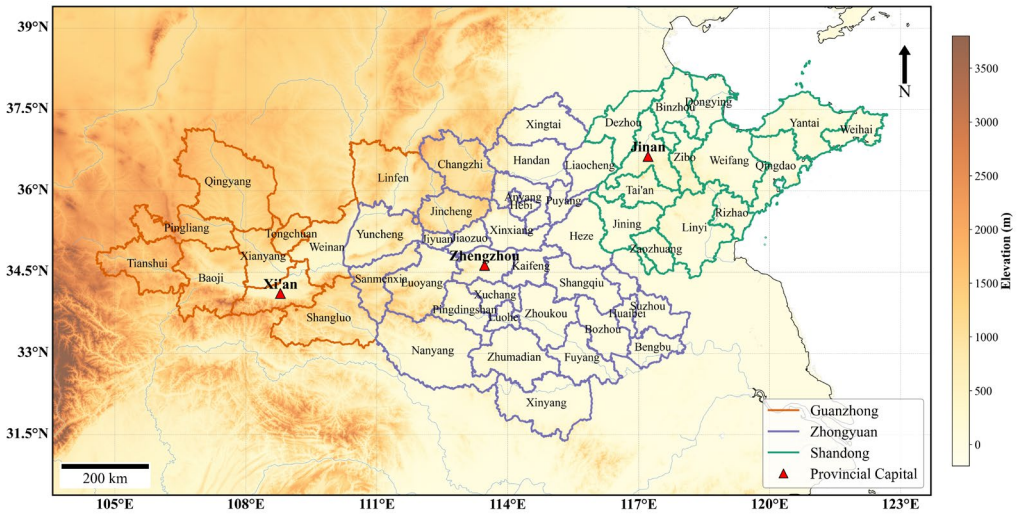


Figure 1. Geographic location and topographic features of the three major urban agglomerations in the middle and lower reaches of the Yellow River Basin.

2.2. Data Source

The $PM_{2.5}$ and other five criteria pollutant datasets used in this study were obtained from the China National Environmental Monitoring Centre (CNEMC) (https://www.cnemc.cn/). In accordance with the Ambient Air Quality Standards (GB 3095-2012) [41], the data were recorded hourly. These monitoring stations are primarily distributed in urban areas and have been widely utilized in atmospheric pollutant monitoring across China. Data preprocessing included the removal of outliers and null values. Daily, monthly, seasonal, and annual averages were subsequently calculated using the arithmetic mean method. Data analysis was performed using Python (v3.13) and R (v4.3.3).

To analyze the factors influencing the spatiotemporal distribution of pollutants, multiple datasets were collected. Meteorological factors, including air temperature, atmospheric pressure, precipitation, and relative humidity, were derived from the China High-resolution Multi-element Meteorological Forcing Product (China Met). This dataset was developed by integrating multi-source remote sensing data, reanalysis products, and observational data from over 2000 meteorological stations, offering a spatial resolution of 1 km and temporal resolutions at daily, monthly, and annual scales [42]. In this study, annual data were averaged to obtain multi-year mean values.

Digital Elevation Model (DEM) data were obtained from the Copernicus DEM, which provides a 30 m spatial resolution and is recognized as one of the highest-quality open-source global DEM products. In this study, the DEM for the research area was extracted via mask extraction based on the shapefile (shp) boundaries of the three major urban agglomerations in the YRB. Slope data were subsequently derived from the DEM.

Population data were sourced from the WorldPop 1 km resolution global dataset, which was resampled and mosaicked from the 100 m resolution population count products, covering the period from 2015 to 2030. Solar radiation (Srad) data were obtained from the China Meteorological Forcing Dataset (CMFD). The CMFD 2.0 product features a temporal resolution of 3 h and a horizontal spatial resolution of 0.1°. It integrates the European Centre for Medium-Range Weather Forecasts (ECMWF) ERA5 reanalysis data with surface station observations, specifically incorporating artificial intelligence techniques for radiation and precipitation products.

2.3. Analytical Methods

2.3.1. Sen's Slope Estimator and Mann–Kendall Test for Trend Analysis

Sen's slope estimator is a non-parametric method characterized by high computational efficiency and robustness against outliers. It is commonly integrated with the Mann–Kendall (MK) non-parametric test to detect trends in long-term time series. The calculation formula is presented in Equation (1). In this formula, β represents the six criterion pollutants, while x_i and x_j denote the pollutant concentration values in the ith and jth years, respectively (i, j = 1, 2, 3, . . ., n and i > j). The "Median" refers to the median function. A value of $\beta > 0$ indicates an increasing trend in pollutant concentrations within the study area, $\beta = 0$ signifies that the concentrations remained relatively stable during the study period, and $\beta < 0$ denotes a decreasing trend.

$$\beta = \text{Median}\left(\frac{x_j - x_i}{j - i}\right) \quad \forall j > i \tag{1}$$

The Mann–Kendall (MK) significance test is widely employed to evaluate the statistical significance of trends in time-series variables [21]. As a non-parametric approach, it does not require the assumption of normality for data variance, thereby effectively mitigating the influence of outliers on the final results. The MK test is calculated as follows:

$$S = \sum_{i=1}^{n-1} \sum_{j=i+1}^{n} \text{sgn}(x_j - x_i), \tag{2}$$

$$\text{sgn}(x_j - x_i) = \begin{cases} +1 & x_j - x_i > 0 \\ 0 & x_j - x_i = 0 \\ -1 & x_j - x_i < 0 \end{cases}, \tag{3}$$

$$Z = \begin{cases} \frac{S-1}{\sqrt{\text{VAR}(S)}}, & S > 0, \\ 0\ , & S = 0,, \\ \frac{S+1}{\sqrt{\text{VAR}(S)}}, & S < 0. \end{cases} \tag{4}$$

For a given significance level α, a trend is considered statistically significant when $|Z| > z_{1-\alpha/2}$; otherwise, the change is regarded as slight or non-significant. Based on the Z-scores derived from the Mann–Kendall test, the variation trends of atmospheric pollutants are categorized into four levels: significant decrease, non-significant decrease, non-significant increase, and significant increase. Specifically, a value of $|Z| > 1.96$ indicates a significant change at the 95% confidence level ($\alpha = 0.05$). When $0 < |Z| \leq 1.96$, the trend is identified as non-significant.

2.3.2. Partial Correlation Coefficient

The partial correlation coefficient is an indicator used to measure the "pure degree of association" between two variables after eliminating the interference of all other potential

variables. The value of this coefficient ranges from −1 to 1; the closer the absolute value is to 1, the stronger the correlation, whereas a value closer to 0 indicates a weaker correlation. Common methods for calculating partial correlation coefficients include the residual method and the inverse correlation matrix method.

Given that this study requires the calculation of pairwise correlations among six distinct pollutants—involving a large number of variables—the residual method would be computationally inefficient as it necessitates step-by-step calculations. Therefore, the inverse correlation matrix method is adopted for batch computation. Let r_{XY} represent the Pearson correlation coefficient between X and Y; r_{XZ} between X and Z; and r_{YZ} between Y and Z. Then, $r_{XY \cdot Z}$ denotes the partial correlation coefficient between X and Y while controlling for variable Z. The formula for the inverse correlation matrix is as shown in Equation (5):

$$r_{XY \cdot Z} = \frac{r_{XY} - r_{XZ} \cdot r_{YZ}}{\sqrt{(1 - r_{XZ}^2) \cdot (1 - r_{YZ}^2)}}, \quad (5)$$

2.3.3. GeoDetector

GeoDetector is a statistical method designed to detect spatial differentiation of geographical phenomena and reveal their underlying driving mechanisms. In this study, the factor detector and interaction detector modules of GeoDetector were employed to quantify the influence of individual environmental factors on the spatial differentiation of pollutant concentrations and to evaluate the effects of interactions between these factors. To mitigate the uncertainty associated with single-year detection results, this study assessed the driving intensity of various factors regarding the spatial differentiation of $PM_{2.5}$ concentrations comprehensively across the period from 2015 to 2024.

The q-statistic for the factor detector is calculated as shown in Equation (6):

$$q^2 = 1^2 - \left(\sum_{h=1}^{L} N_h \sigma_h^2 \right) / N\sigma^2, \quad (6)$$

q represents the explanatory power (influence) of a driving factor on the spatial differentiation of $PM_{2.5}$ concentrations. Its value ranges within [0, 1], where a higher value indicates a stronger influence of the factor. h = 1, 2, . . ., L denotes the strata (sub-regions) of the explanatory variable X. L denotes the number of strata or classifications for the variable. N and N_h represent the total number of samples in the entire study area and the number of samples in stratum h, respectively. σ^2 and $N\sigma^2$ represent the total variance of the $PM_{2.5}$ concentrations across the entire area and the variance within stratum h, respectively.

3. Results

3.1. Temporal Evolution and Trend Analysis

During the 2015–2024 period, the air quality across the three major urban agglomerations of the YRB improved substantially. As illustrated in Figure 2, five out of the six criterion pollutants exhibited significant downward trends, aligning with the coordinated implementation of regional ecological protection and "Dual Carbon" strategies.

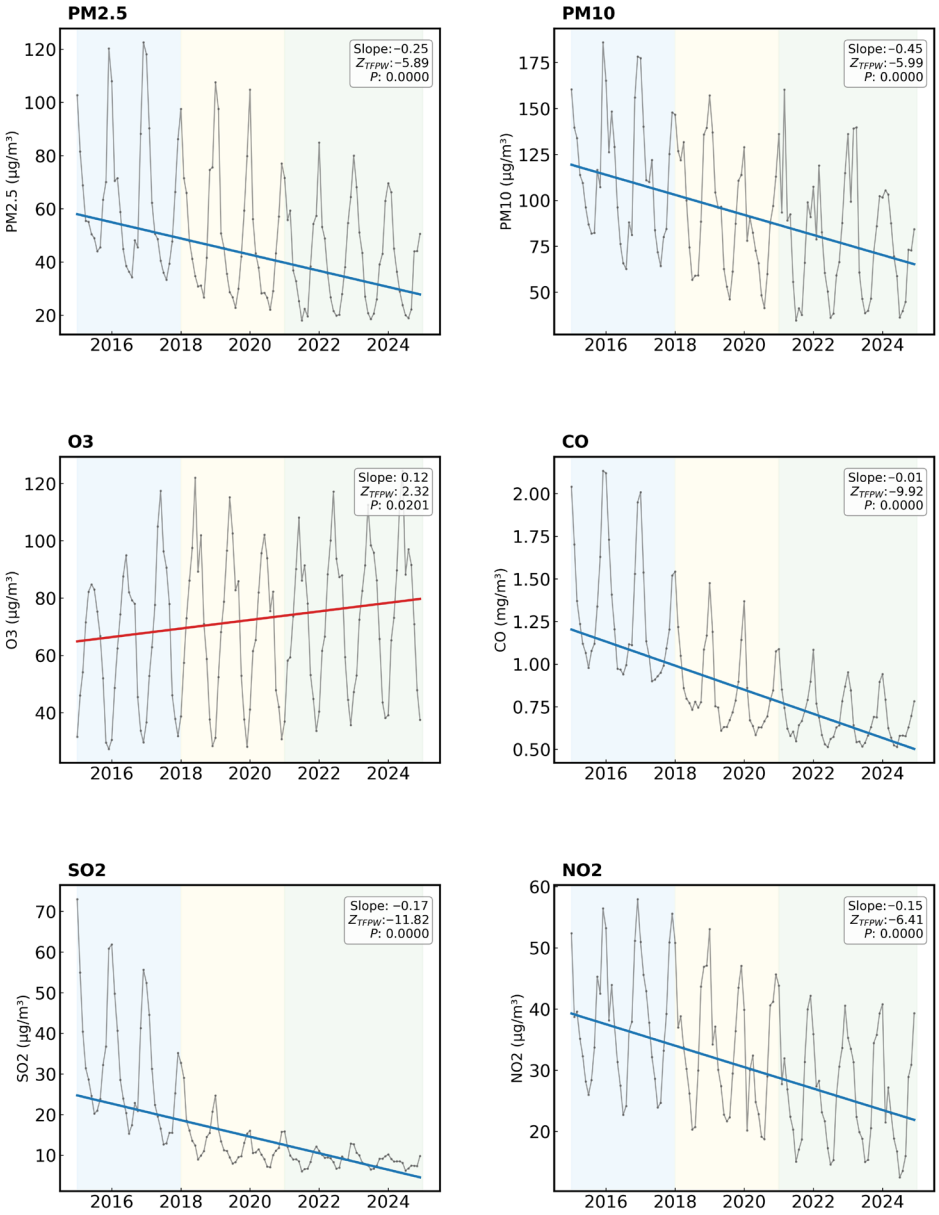


Figure 2. Monthly temporal variations and long-term trends of six criterion air pollutants in the study area from 2015 to 2024. The blue and red solid lines represent the slopes of the Sen's slope analysis, the dotted broken lines denote the long-term changing trends, and the three different background colors indicate the implementation periods of China's air pollution control policies.

3.1.1. Inter-Annual Evolution and Decoupling Trends

Statistical summaries of the inter-annual trends are provided in Table 1. $PM_{2.5}$, PM_{10}, NO_2, SO_2, and CO all demonstrated significant monotonic decreasing trends ($p < 0.001$). Notably, SO_2 concentrations exhibited the most dramatic decline, with a Mann–Kendall Z-score of −10.28 and a reduction exceeding 80% over the decade. This plummet in SO_2 is primarily attributed to the stringent implementation of "coal-to-gas" conversion projects and the widespread upgrading of industrial desulfurization facilities across the mid–lower reaches of the basin. Similarly, $PM_{2.5}$ dropped from an annual average of 67.27 $\mu g/m^3$ in 2015 to 39.29 $\mu g/m^3$ in 2024 (slope = −0.25). During the period from 2015 to 2024, O_3 concentrations exhibited an upward trend (slope = 0.12, Z = 2.32, $p = 0.02$). The highest O_3 levels occurred in summer throughout the year. In the Mann–Kendall test, the Z-value was slightly below 1.96 and the p-value slightly above 0.05, which undermines the persuasiveness of interpreting the trend as statistically significant.

Table 1. Mean concentrations in 2015 and 2024 (averaged across monitoring sites) and corresponding long-term trend statistics (Sen's slope; Mann–Kendall Z and *p*) for six criterion air pollutants (2015 to 2024).

Pollutant	Mean (2015)	Mean (2024)	Sen's Slope	M-K(Z)	*p*-Value
$PM_{2.5}$ ($\mu g/m^3$)	67.27	39.29	−0.25	−4.21	<0.001
SO_2 ($\mu g/m^3$)	37.38	8.11	−0.17	−5.13	<0.001
O_3 ($\mu g/m^3$)	58.61	77.97	0.12	2.32	0.02
CO (mg/m^3)	1.40	0.65	−0.01	−3.95	<0.001
NO_2 ($\mu g/m^3$)	38.20	24.07	−0.15	−4.08	<0.001

3.1.2. Seasonal Variation Patterns

Figure 2 shows pronounced seasonality for $PM_{2.5}$, PM_{10}, CO, NO_2, O_3 and SO_2, with winter maxima and summer minima across the three urban agglomerations. For example, wintertime $PM_{2.5}$ in 2015 averaged 101.76 $\mu g/m^3$, substantially higher than the corresponding summer level. This pattern is consistent with enhanced emissions during the heating season and less favorable dispersion conditions in winter. In the summer of 2015, O_3 concentration was 80.92 $\mu g/m^3$, peaked at 111.91 $\mu g/m^3$ in the summer of 2022, and then showed a declining trend, reaching 104.58 $\mu g/m^3$ in the summer of 2024. Notably, while PM_{10} reached a decade low in 2022 (96.26 $\mu g/m^3$), a slight rebound was observed thereafter. This likely reflects the rapid recovery of regional infrastructure investment and industrial production activities in the post-pandemic era.

3.2. Spatial Characterization and Seasonal Variations in Multi-Pollutant Concentrations

The six criterion pollutants exhibit pronounced spatial heterogeneity and distinct seasonal disparities across the three major urban agglomerations of the YRB. Overall, high-value clusters of $PM_{2.5}$, PM_{10}, CO, NO_2, O_3 and SO_2 are primarily concentrated in the CPUA and the western portion of the SPUA. In contrast, relatively lower concentrations are observed in the GZPUA and the coastal areas of the SPUA. This spatial gradient is likely linked to the high density of industrial emissions and population in the central plains, coupled with the "cleansing effect" of maritime air masses in coastal regions [43–45]. Furthermore, SO_2 hotspots are localized in a few energy-intensive industrial cities, while O_3 displays a spatial pattern nearly inverse to that of particulate matter ($PM_{2.5}$ and PM_{10}), with higher values emerging in parts of the eastern SPUA and central-eastern regions.

3.2.1. Seasonal Dynamics and Regional Gradients of Key Air Pollutants

At the seasonal scale, as shown in Figures 3 and 4, $PM_{2.5}$ and PM_{10} distributions typically follow an increasing southwest-to-northeast gradient during the annual, spring, autumn, and winter periods. During autumn and winter, high-concentration zones form continuous, large-scale clusters. This spatial continuity suggests significant regional transport and the "trapping effect" of the basin's complex topography during periods of atmospheric stability [46,47]. In summer, overall concentrations decrease substantially, and the spatial extent of high-value zones contracts significantly, persisting only at moderate levels in specific central cities. Conversely, the spatial distribution of O_3 is characterized by a "high in summer/east and low in winter/west" pattern. During summer, a continuous high-value belt forms across the SPUA and central cities. This eastward-increasing gradient reflects the synergy between higher precursor (NOx and VOCs) concentrations and stronger solar radiation in the eastern plains compared to the western highlands. This range contracts slightly during spring and autumn and remains at a low baseline level across the entire region in winter.

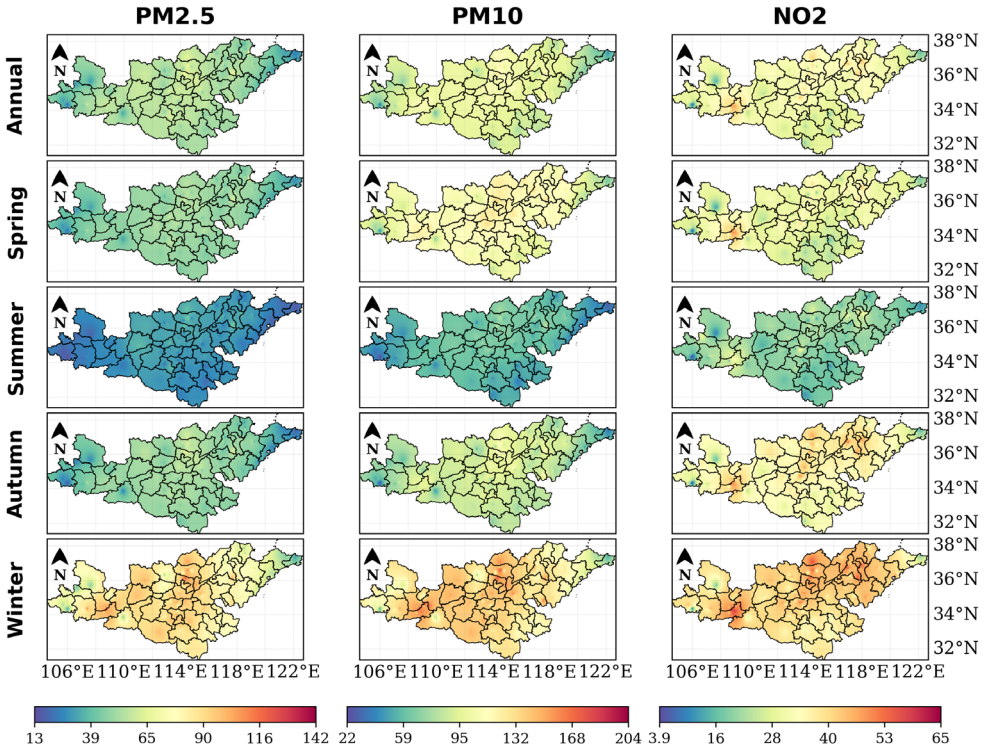


Figure 3. Annual and seasonal spatial distribution of $PM_{2.5}$ ($\mu g/m^3$), PM_{10} ($\mu g/m^3$), and NO_2 ($\mu g/m^3$) concentrations across the three major urban agglomerations in the Yellow River Basin.

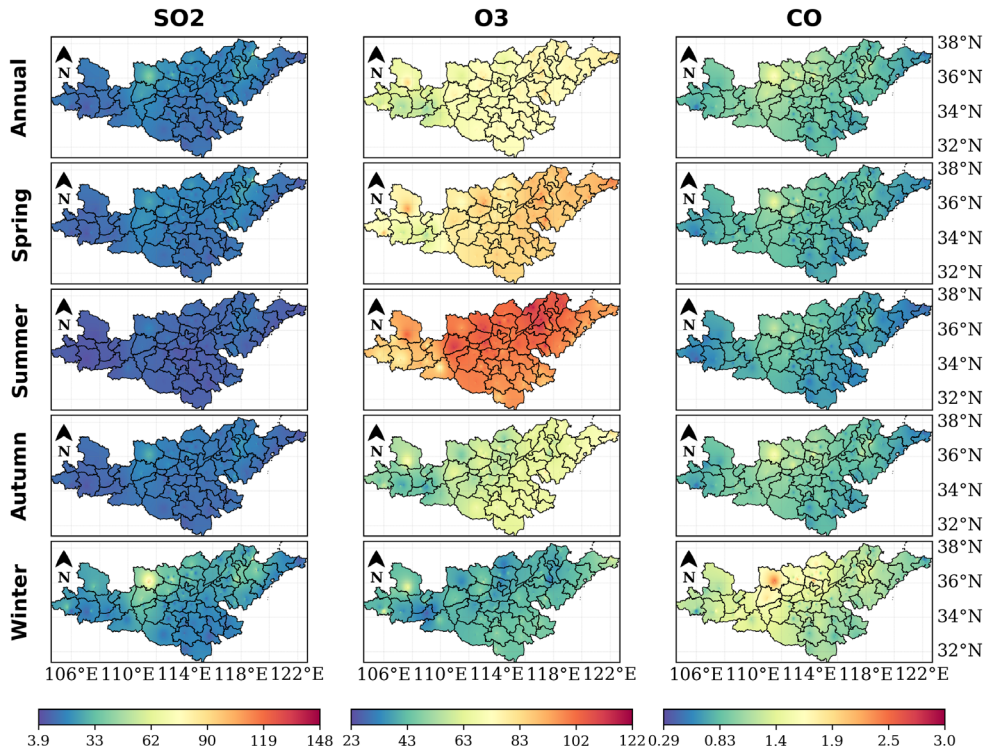


Figure 4. Annual and seasonal spatial distribution of SO_2 ($\mu g/m^3$), O_3 ($\mu g/m^3$) and CO (mg/m^3) concentrations across the three major urban agglomerations in the Yellow River Basin.

The spatial distribution of NO_2 annually and in winter closely mirrors that of $PM_{2.5}$, with the core of the CPUA and cities with dense transportation networks serving as prominent hotspots. The spatial overlap between NO_2 peaks and major traffic corridors highlights the dominant contribution of vehicular emissions to urban air pollution [48–50].

In summer, NO_2 levels weaken overall, leaving only linear high-value ribbons along primary transportation axes. SO_2 distribution is dominated by localized hotspots across all seasons. Annual and winter high-value centers are concentrated in specific cities characterized by coal-fired power plants or heavy chemical industries. During summer and autumn, the overall concentration decreases, and spatial variance diminishes.

3.2.2. Spatial and Seasonal Patterns of Temporal Trend Slopes of Air Pollutants

On an annual scale, as shown in Figures 5 and 6, the most significant negative slopes (indicating the fastest improvement) for $PM_{2.5}$ and PM_{10} were concentrated in the eastern portion of the CPUA and western Shandong Province, where localized stations exhibited substantial reduction rates. In contrast, the negative slopes in the GZPUA and coastal areas of Shandong were relatively smaller, forming a spatial gradient described as "gradually weakening from east to west and from core cities to the periphery." The more pronounced decreases in NO_2 and CO were concentrated within urban areas. For $PM_{2.5}$, PM_{10}, NO_2, and CO, negative slopes were more evident in spring, autumn, and winter, whereas the magnitude of decrease tended to be smaller in summer. In winter, several core urban areas exhibited the most significant declines, aligning with strengthened emission control measures during the heating season, though interannual meteorological variations may also be a contributing factor. The positive values in portions of the central-eastern and coastal regions were slightly higher in summer than in other seasons. Consequently, these areas represent critical focus zones for future synergistic control strategies targeting both particles and ozone.

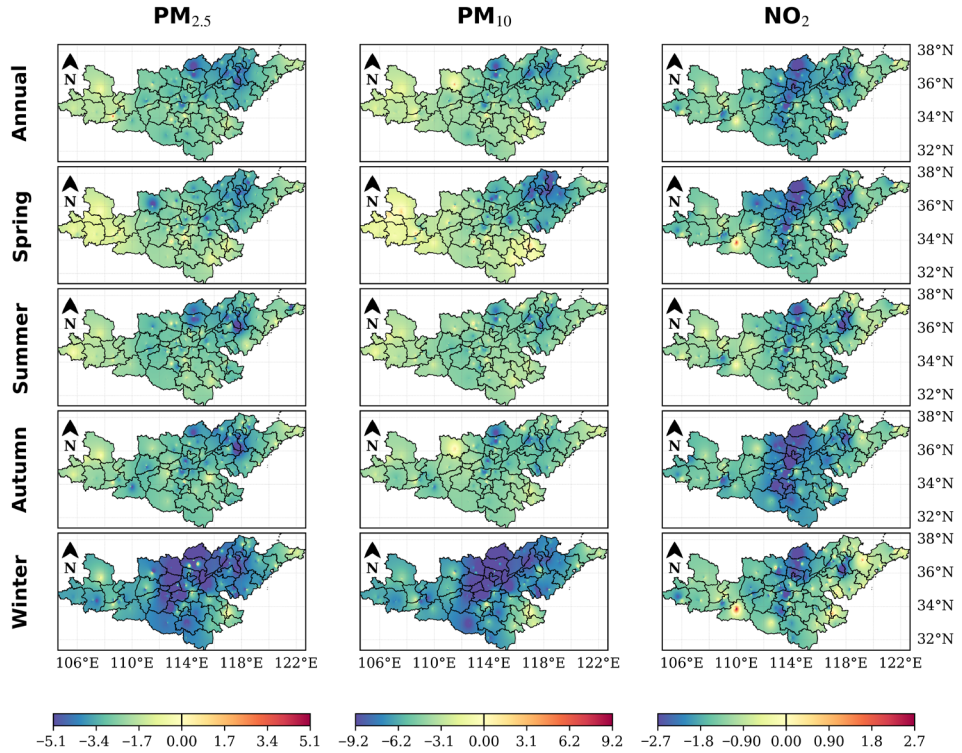


Figure 5. Spatial distribution of Sen's slope for annual and seasonal trends of $PM_{2.5}$ ($\mu g/m^3$), PM_{10} ($\mu g/m^3$), and NO_2 ($\mu g/m^3$) across the three major urban agglomerations.

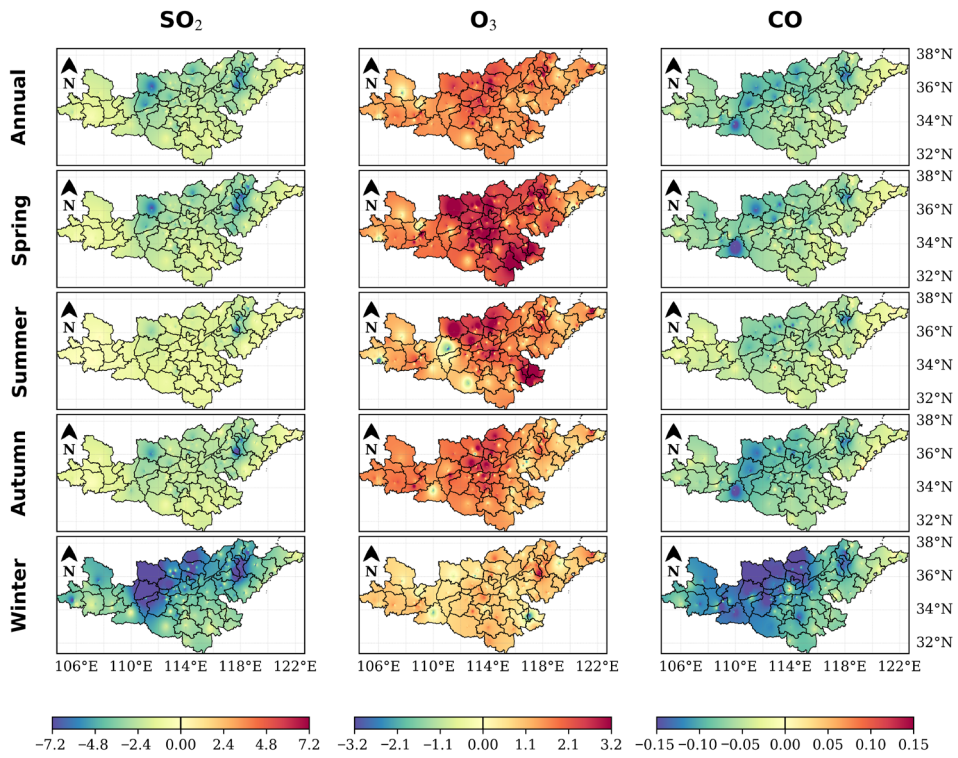


Figure 6. Spatial distribution of Sen's slope for annual and seasonal trends of SO_2 (μg/m^3), O_3 (μg/m^3) and CO (mg/m^3) across the three major urban agglomerations.

3.2.3. Results Comparison with Other Regions

Compared with studies from other regions, the spatiotemporal patterns identified in the three YRB urban agglomerations are broadly consistent with the global picture of decreasing particulate pollution and persistent or increasing ozone. In Europe, long-term analyses in Germany and Italy have reported significant declines in $PM_{2.5}$ and PM_{10} following stringent emission controls, while surface O_3 trends are mixed, with many urban sites showing either weak increases or only limited decreases, particularly in warm seasons [51,52]. Similar behavior has been documented in the United States, where NO_x and primary PM emissions have fallen under the Clean Air Act, yet summertime O_3 formation in regions such as California remains problematic because of non-linear NO_x–VOC chemistry and meteorological sensitivity [53,54]. In rapidly urbanizing India, recent work has shown strong reductions or stabilization of $PM_{2.5}$ in some cities but continued high levels and frequent exceedances of WHO guidelines, accompanied by rising O_3 exposure risks linked to increasing anthropogenic VOCs and intense photochemistry [55,56]. By contrast, Japan and South Korea—both of which have implemented long-term national and regional air-pollution control strategies—generally exhibit declining $PM_{2.5}$ concentrations and more moderate O_3 trends, although positive O_3 tendencies are still observed in several urban areas [57]. Overall, the YRB pattern of marked wintertime reductions in primary pollutants but weakly increasing, meteorology-sensitive O_3, especially in coastal and downwind regions, aligns more closely with the experience of East Asian and some European city clusters than with that of North America, underscoring the need for synergistic $PM_{2.5}$–O_3 control that explicitly accounts for regional transport and season-specific photochemical regimes.

3.3. Partial Correlation Analysis Among the Six Criterion Air Pollutants

The spatial distribution and inter-pollutant correlations vary across the three major urban agglomerations due to differences in geographical location (land–sea distribution)

and socio-economic conditions. By analyzing the partial correlation coefficients among the six criterion pollutants, strong associations were identified within particulate matter categories and between particulates and combustion-related gases [58,59].

The partial correlation coefficients for $PM_{2.5}$–PM_{10} in the GZPUA, CPUA, and SPUA were 0.67, 0.78, and 0.73, respectively, all showing significant positive correlations, as shown in Figure 7. This indicates that the two types of particulate matter are highly coupled in terms of sources and transport processes, co-regulated by primary emissions and secondary particle formation. The $PM_{2.5}$–CO correlation was prominent in the CPUA (0.65) and SPUA (0.69). Combined with the moderate negative correlations observed for PM_{10}–CO (−0.19 to −0.47), these results suggest that fine particles and carbon monoxide are markedly influenced by combustion sources. The inverse relationship between coarse particles and CO in certain regions may be linked to dust/fugitive dust processes and varying meteorological conditions.

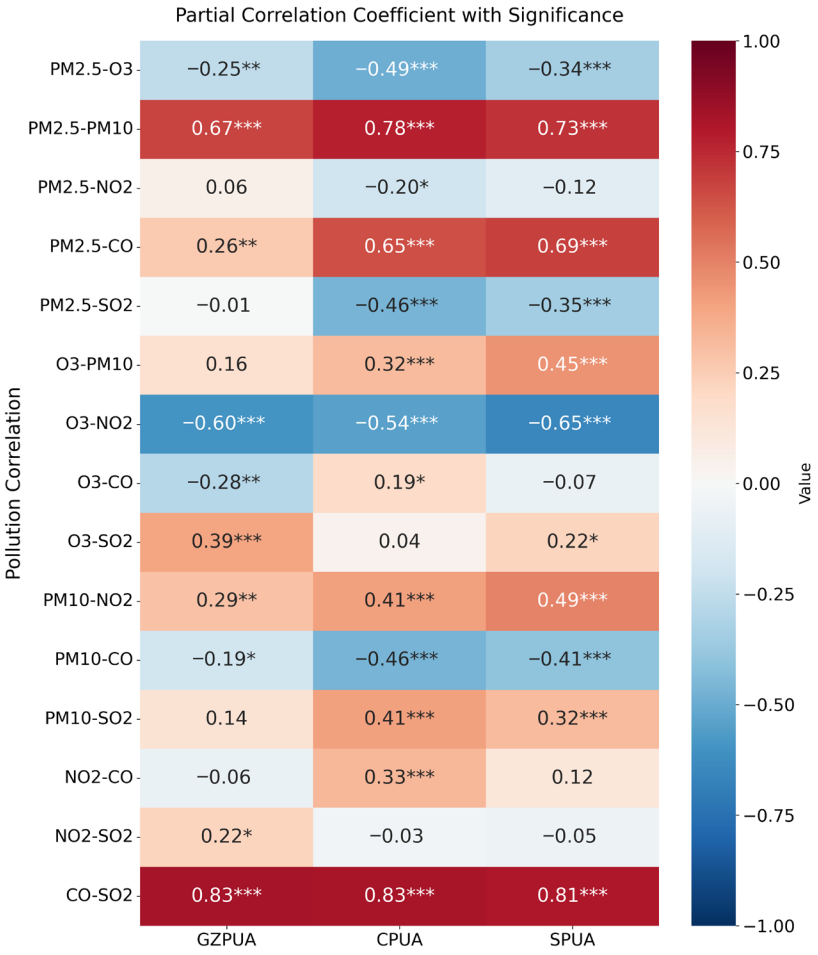


Figure 7. Partial-correlation heatmap for pairwise criterion air pollutants in the three major urban agglomerations (*** $p < 0.001$, ** $p < 0.01$, * $p < 0.05$).

O_3 exhibited inverse correlations with its precursor gases. The O_3–NO_2 partial correlation coefficients across the three regions were −0.60, −0.54, and −0.65, representing strong negative associations. This reflects the dual role of NO_2 as a vital O_3 precursor and a participant in the photochemical equilibrium that titrates O_3 [60,61]. O_3–$PM_{2.5}$ showed moderate negative correlations (−0.25 to −0.49), consistent with the previously discussed trend of "declining $PM_{2.5}$ and slowly rising O_3". Regional disparities in O_3–CO correlations (−0.28 to 0.19) suggest that CO may act as a weak precursor in some regions while being modulated by boundary layer structures and transport conditions in others.

The $PM_{2.5}$–NO_2 relationship was weak overall and varied from −0.20 to 0.06, suggesting that the association between NO_2 and $PM_{2.5}$ differs with secondary formation conditions and local emission characteristics. The $PM_{2.5}$–SO_2 correlation was close to zero in the GZPUA (−0.01) but became clearly negative in the CPUA (−0.46) and SPUA (−0.35). One possible explanation is that coal-reduction efforts in the Central Plains and the Shandong Peninsula have reduced the co-variation between SO_2 and secondary PM. By comparison, PM_{10}–SO_2 remained weak to moderately positive (0.14–0.41), which may be related to a mix of coal combustion emissions and industrial dust contributions.

3.4. Analysis of Influencing Drivers Based on GeoDetector

In this study, nine influencing factors were selected to quantify the contribution of each factor to the pollutants. The data format is described in Section 2.2. Given the inherent correlation between Digital Elevation Model (DEM) and Slope Aspect, the spatial distribution map for Aspect is not redundantly displayed in the text. In the data preprocessing phase, a long-term averaging treatment was applied to the nine categories of data from 2015 to 2024. This approach was adopted to eliminate the influence of inter-annual fluctuations on the established spatial patterns. The spatial distributions of the eight representative driving factors within the study area exhibit significant spatial stratified heterogeneity (Figure 8). For the purpose of simplifying subsequent analysis, the factors are defined as follows: Wind Speed (Wind, X1), Temperature (TMP, X2), Solar Radiation (SRAD, X3), Relative Humidity (RHU, X4), Atmospheric Pressure (PRES, X5), Precipitation (PREC, X6), Aspect (X7), Population Density (POP, X8), and Elevation (DEM, X9).

The q-statistic of the factor detector indicates that for particulate matter ($PM_{2.5}$ and PM_{10}), the top four driving factors, in order, are wind speed (X1, q = 0.30), temperature (X2, q = 0.27), elevation (X9, q = 0.23), and atmospheric pressure/precipitation (X5/X6, q = 0.20), suggesting that the spatial variation in particulate matter is closely related to large-scale circulation conditions and underlying surface topographic features. For ozone (O_3), which is most sensitive to photochemical reaction conditions and boundary layer structure, the dominant factors are wind speed (X1, q = 0.44), elevation (X9, q = 0.37), atmospheric pressure (X5, q = 0.37), and solar radiation (X3, q = 0.37).

Seasonally, in summer, O_3 shows the strongest response to radiation (X3) and temperature (X2) (q = 0.47), consistent with its dependence on high temperatures and strong radiation conditions. In autumn and winter, $PM_{2.5}$ and PM_{10} revert to a pattern dominated by wind speed and temperature (X1, X2; q = 0.32), highlighting the influence of atmospheric stability and heating-season emissions. Conversely, in winter, SO_2 and CO are primarily driven by relative humidity and precipitation (X4, X6; q = 0.54), emphasizing the role of humidity-related scavenging processes and regional emission structures.

The interaction detector shows that, for paired factors, the interaction q value is higher than the q value of either factor alone, corresponding to a bi-factor enhancement effect. This suggests that pollutant patterns across the three urban agglomerations are associated with multiple drivers acting together rather than one dominant factor. On an annual scale, the highest explanatory power for particulate matter ($PM_{2.5}$ and PM_{10}) was observed in the combinations of Precipitation ∩ Temperature (X6 ∩ X2, q = 0.64) and Elevation ∩ Temperature (X9 ∩ X2, q = 0.61), followed by Wind Speed ∩ Temperature (X1 ∩ X2, q = 0.60). These results indicate that temperature, atmospheric humidity, and precipitation have a joint influence on the spatial distribution of particulate matter. For ozone (O_3), the strongest interactions are radiation ∩ temperature (X3 ∩ X2, q = 0.68) and precipitation ∩ radiation (X6 ∩ X3, q = 0.66), indicating that radiative and thermal conditions, together with humidity-related processes, are all related to the spatial pattern of ozone. For sulfur dioxide (SO_2) and carbon monoxide (CO), the highest interaction q values occur in

humidity combinations related to wind speed or temperature (X4 ∩ X1/X4 ∩ X2, q = 0.71), indicating that these combustion-related pollutants often have higher concentrations under humid conditions, especially when dispersion is relatively weak.

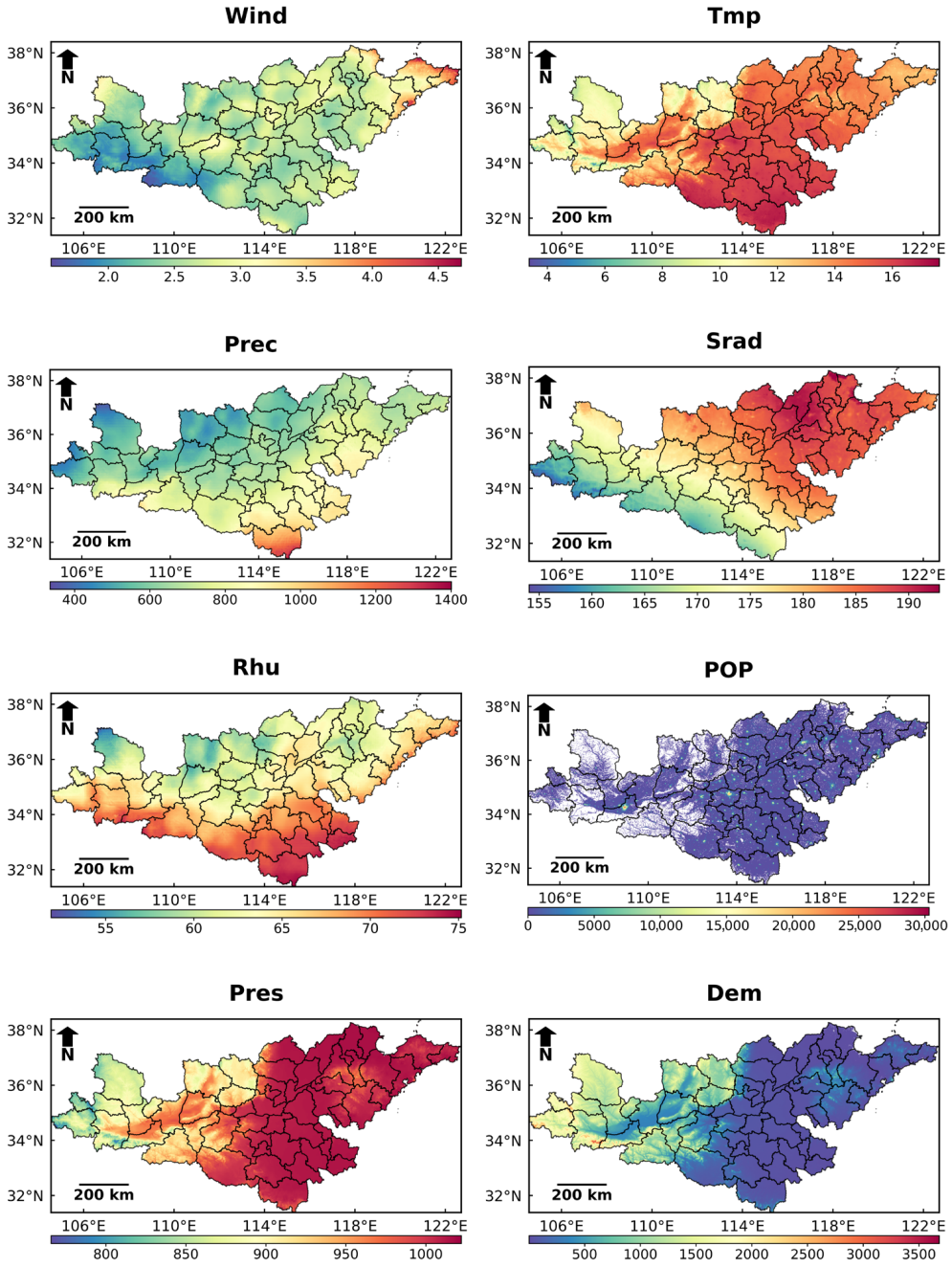


Figure 8. Spatial distribution patterns of the eight potential driving factors within the three major urban agglomerations of the Yellow River Basin.

In spring, O_3 showed the strongest interaction effects for Radiation ∩ Temperature and Elevation ∩ Radiation (X3 ∩ X2 and X6 ∩ X3; q = 0.73). This pattern is in line with springtime conditions when radiation increases and atmospheric mixing becomes more active. In summer, O_3 was still mainly associated with Radiation ∩ Temperature and Elevation ∩ Radiation (X3 ∩ X2 and X9 ∩ X3; q = 0.71), indicating that radiative and thermal conditions remain important for ozone-related interactions. In autumn, the leading interactions for particulate matter and NO_2 shifted to Pressure ∩ Temperature and Wind Speed ∩ Temperature (X5 ∩ X2 and X1 ∩ X2; q = 0.63), suggesting a larger role of stable meteorological

conditions during the seasonal transition. In winter, when pollution episodes are more frequent during the heating period, interactions involving stability-related variables (e.g., low wind and higher pressure) together with humidity and precipitation showed relatively high explanatory power. For $PM_{2.5}$ and PM_{10}, q reached 0.67 under Pressure ∩ Temperature and Elevation ∩ Temperature. The detailed data descriptions are provided in Appendix A.

4. Discussion

This study analyzed the spatiotemporal distribution patterns of air pollutants across three urban agglomerations in the YRB from 2015 to 2024, utilizing partial correlation analysis and the GeoDetector model. The results indicate that particulate matter ($PM_{2.5}$ and PM_{10}) and gaseous pollutants (NO_2, SO_2, CO) exhibited downward trends; O_3 concentrations followed an upward trend, peaking annually during the summer.

The observed decline in most pollutants aligns with previous studies focusing on the YRB, the Central Plains, the Guanzhong Plain, and key cities such as Xi'an and Zhengzhou [62–64]. These improvements are attributable to the stringent air pollution prevention and control policies implemented since 2013, alongside advancements in industrial governance and traffic management [65]. The rising trend of O_3 as particulate levels are brought under control is consistent with recent nationwide observations. Wang and Liu et al. have identified O_3 as a primary target for future atmospheric governance in China [66,67]; the choice of discretization method and the number of classes is a key step affecting the robustness of GeoDetector results. Existing research has provided methodological references, generally suggesting 5–8 classes and commonly adopting equal-interval or natural-break schemes for factor discretization in GeoDetector applications [68–72]. We conducted a sensitivity analysis of different classification methods and class numbers (see Supplementary Materials for details). We found that the natural-break classification with nine classes produced more stable and higher explanatory performance across pollutants and seasons.

The stronger interaction between elevation and radiation further suggests that topography modifies both the radiative environment and vertical exchange, amplifying O_3 formation and accumulation at higher altitudes [73,74]. Observations along elevation gradients and at high-altitude or mountainous sites have documented enhanced spring O_3 linked with stronger background radiation, more frequent coupling with the free troposphere, and more efficient vertical mixing, again pointing to a non-linear combined effect of elevation and radiative forcing on surface O_3 [75,76].

Partial correlation analysis revealed a significant positive correlation between $PM_{2.5}$ and PM_{10}. A strong negative correlation exists between O_3 and NO_2, reflecting the role of NO_2 as a critical precursor and the titration effect in the photochemical cycle [77]. While $PM_{2.5}$ and O_3 are negatively correlated across the three regions, PM_{10} and O_3 exhibit a positive correlation, particularly in the coastal Shandong Peninsula. The "declining PM/rising O_3" phenomenon is a pivotal shift in China's pollution landscape, necessitating research into co-existence and synergistic governance to support high-quality regional development [78]. NOx requires close attention not only as a primary pollutant but as a driver of secondary inorganic aerosol formation through interactions with volatile organic compounds (VOCs). Future strategies must prioritize the synergistic control of multiple pollutants [79]. By targeting emissions co-emitted with CO_2, we can simultaneously improve air quality and reduce carbon emissions, thereby serving the national "Dual Carbon" strategic goals.

5. Conclusions

Using station-based daily observations from 2015 to 2024, this study quantified trends, seasonality, spatial heterogeneity, and key drivers of six criterion pollutants across the Guanzhong Plain, Central Plains, and Shandong Peninsula urban agglomerations in the middle–lower YRB. Based our findings, we observed that $PM_{2.5}$, PM_{10}, NO_2, SO_2, and CO generally decreased over the study period, whereas O_3 showed a weak increasing tendency with pronounced summer maxima. Spatially, higher particulate matter and combustion-related pollutants were concentrated in the core areas of the Central Plains urban agglomeration (e.g., Zhengzhou and Xinxiang), while elevated O_3 occurred more frequently in coastal areas and parts of the Shandong Peninsula region. GeoDetector results indicate that meteorological conditions—especially wind speed and temperature and their interactions with precipitation/topography—provide the strongest explanatory power for pollutant heterogeneity, highlighting the importance of season-specific mechanisms. These results suggest that future control policies should jointly address wintertime PM reduction and summertime ozone formation, with coordinated strategies tailored to the distinct regional contexts of the three urban agglomerations. In daily practice, this implies region-oriented, multi-pollutant management that simultaneously considers local emissions, regional transport and meteorology. Evidence from other major Chinese urban agglomerations shows that joint $PM_{2.5}$–O_3 control can yield substantial additional health and economic benefits compared with single-pollutant strategies, but requires differentiated reduction pathways for NOx, VOCs, SO_2 and primary PM across cities. For the middle–lower YRB, the findings here suggest several actionable directions. First, in the Central Plains UA, where particulate pollution remains highest, continued deep cuts in primary $PM_{2.5}$, SO_2 and NOx from heavy industry and wintertime residential combustion should be prioritized, while preventing NOx-only control from exacerbating summertime O_3 under VOC-limited regimes. Second, in the coastal and Shandong Peninsula UAs, where O_3 burdens and meteorological sensitivity are stronger, emission reduction should focus more on VOCs from industry and solvents, coordinated with region-wide NOx control and seasonal O_3-targeted measures in spring–summer. Third, across all three urban agglomerations, cross-boundary joint-prevention mechanisms are needed to address strong spillover and transport identified in other clusters such as the Beijing–Tianjin–Hebei Urban Agglomeration and YRD regions, including shared early warning, unified emission-reduction schedules during regional episodes, and city-cluster-level health-risk assessments to guide period- and pollutant-specific interventions.

Supplementary Materials: The following supporting information can be downloaded at https://www.mdpi.com/article/10.3390/atmos17030242/s1: Figure S1. Sensitivity of factor detector results to discretization method and number of strata, $PM_{2.5}$—annual (folder "results1"), O_3—annual (folder "results2"), O_3—summer (folder "results3"), $PM_{2.5}$—winter (folder "results4").

Author Contributions: Conceptualization, Y.Y.; methodology, Q.H. and F.Z.; software, F.Z., and Q.H.; validation, F.Z., J.L. and Q.W.; formal analysis, L.S. and Y.L.; investigation, P.W.; data curation, T.C., Z.Z. and M.Z.; writing—original draft preparation, F.Z.; writing—review and editing, Y.Y. and F.Z.; visualization, R.H. and Z.L.; project administration, Q.H.; funding acquisition, Q.H. All authors have read and agreed to the published version of the manuscript.

Funding: This research was supported by the National Natural Science Foundation of China (Nos. 42277478, U21A20109, 52274165), the National Key Research and Development Program of China (No. 2024YFC3212200), the Henan Science Foundation for Distinguished Young Scholars of China (No. 242300421041), the Henan Provincial University Science and Technology Innovation Team Support Program (No. 25IRTSTHN008), the Henan Key Research and Development Program of China (No. 241111321100); the Joint Fund Project of the Henan Provincial Science and Technology

Research and Development Program (No. 242103810099); and the General Project of Humanities and Social Sciences Research in Henan Provincial Universities (No. 2025-ZZJH-172). The authors would like to thank the editor and reviewers for their contributions to the paper.

Institutional Review Board Statement: Not applicable.

Informed Consent Statement: Not applicable.

Data Availability Statement: Data are contained within the article.

Acknowledgments: We would like to express our respect and gratitude to the anonymous reviewers and editors for their professional comments and suggestions.

Conflicts of Interest: The author declares no conflicts of interest.

Abbreviations

The following abbreviations are used in this manuscript:

YRB	Yellow River Basin
SPUA	Shandong Peninsula Urban Agglomeration
GZPUA	Guanzhong Plain Urban Agglomeration
CPUA	Central Plains Urban Agglomeration

Appendix A

Table A1. Detailed results of the factor detector (q-statistic) for six criterion air pollutants across different seasons and on an annual scale.

	$PM_{2.5}$		PM_{10}		O_3		NO_2		SO_2		CO	
	q	**p**	**q**	**p**	**q**	**p**	**q**	**p**	**q**	**p**	**q**	**p**
Annual	X1 0.30	0	X2 0.27	0	X1 0.44	0	X2 0.28	0	X4 0.50	0	X4 0.42	0
	X2(0.30)	0	X1 0.25	0	X9 0.37	0	X4 0.22	0	X6 0.21	0	X6 0.37	0
	X9(0.21)	0	X9 0.16	0	X5 0.37	0	X6 0.15	0	X2 0.20	0	X5 0.34	0
	X5 0.20	0	X5 0.16	0	X3 0.37	0	X3 0.12	0	X3 0.14	0	X9 0.33	0
Spring	X2 0.36	0	X4 0.26	0	X1 0.44	0	X2 0.25	0	X4 0.41	0	X4 0.42	0
	X1 0.31	0	X2 0.24	0	X3 0.44	0	X4 0.20	0	X3 0.24	0	X5 0.34	0
	X5 0.24	0	X1 0.20	0	X9 0.43	0	X5 0.16	0	X2 0.21	0	X9 0.33	0
	X9 0.23	0	X6 0.17	0	X5 0.42	0	X9 0.16	0	X5 0.14	0	X6 0.30	0
Summer	X4 0.26	0	X2 0.30	0	X3 0.47	0	X2 0.22	0	X4 0.27	0	X4 0.40	0
	X1 0.22	0	X1 0.21	0	X1 0.30	0	X4 0.20	0	X3 0.24	0	X5 0.29	0
	X2 0.19	0	X4 0.17	0	X4 0.25	0	X6 0.18	0	X2 0.19	0	X9 0.28	0
	X9 0.17	0	X6 0.16	0	X2 0.20	0	X5 0.11	0	X5 0.16	0	X6 0.27	0
Autumn	X1 0.33	0	X2 0.30	0	X5 0.47	0	X2 0.28	0	X4 0.40	0	X4 0.39	0
	X2 0.32	0	X1 0.27	0	X9 0.46	0	X4 0.20	0	X3 0.19	0	X6 0.33	0
	X9 0.20	0	X9(0.17)	0	X1 0.42	0	X3 0.17	0	X2 0.13	0	X5 0.32	0
	X5 0.18	0	X5 0.17	0	X3 0.30	0	X6 0.12	0	X6 0.12	0	X9 0.31	0
Winter	X1 0.32	0	X1 0.31	0	X2(0.22)	0	X2 0.35	0	X4 0.54	0	X6 0.45	0
	X2 0.28	0	X2 0.22	0	X6 0.16	0	X4 0.21	0	X6 0.35	0	X4 0.41	0
	X9 0.23	0	X9 0.21	0	X1 0.15	0	X3 0.17	0	X2 0.25	0	X5 0.35	0
	X5 0.19	0	X5 0.19	0	X5 0.14	0	X6 0.13	0	X5 0.19	0	X9 0.35	0

Table A2. Results of the interaction detector (q-statistic) for six criteria air pollutants on annual and seasonal scales.

	$PM_{2.5}$	PM_{10}	O_3	NO_2	SO_2	CO
Annual	X5X2(0.64)	X5X2(0.61)	X3X2(0.68)	X6X2(0.49)	X4X1(0.63)	X6X3(0.71)
	X2X1(0.60)	X6X2 0.59	X6X3 0.66	X5X4 0.48	X4X2 0.63	X5X4 0.64
	X9X2(0.61)	X9X2 0.59	X9X3 0.64	X9X4 0.48	X4X3 0.62	X6X5 0.64
	X5X1(0.58)	X2X1 0.56	X5X3 0.63	X2X1 0.45	X5X4 0.62	X9X4 0.63
Spring	X4X2 0.63	X4X2 0.60	X6X3 0.73	X9X4 0.50	X4X2 0.63	X6X3 0.67
	X5X2 0.63	X5X2 0.59	X3X2 0.73	X5X4 0.50	X4X3 0.62	X4X3 0.64
	X2X1 0.63	X2X1 0.26	X9X3 0.69	X6X2 0.44	X5X4 0.61	X9X4 0.62
	X5X1 0.60	X4X1 0.55	X6X1 0.64	X9X3 0.44	X9X4 0.59	X5X3 0.62
Summer	X4X2 0.61	X4X2 0.61	X3X2 0.71	X9X4 0.48	X4X3 0.56	X6X3 0.67
	X4X1 0.57	X4X1 0.58	X9X3 0.69	X5X4 0.47	X4X2 0.54	X4X3 0.62
	X6X3 0.53	X6X1 0.56	X9X4 0.68	X6X3 0.45	X6X3 0.53	X9X4 0.60
	X2X1 0.54	X6X3 0.56	X4X3 0.68	X4X3 0.45	X5X3 0.52	X5X4 0.60
Autumn	X5X2 0.63	X5X2 0.58	X6X1 0.71	X6X2 0.50	X4X2 0.60	X6X3 0.68
	X2X1 0.62	X2X1 0.57	X6X3 0.71	X9X4 0.46	X4X1 0.59	X4X3 0.62
	X9X2 0.61	X9X2 0.56	X3X20.67	X2X1 0.46	X5X4 0.55	X5X4 0.61
	X5X2 0.59	X6X2 0.56	X9X4 0.66	X5X4 0.46	X4X3 0.55	X6X5 0.61
Winter	X5X2 0.67	X5X2 0.65	X6X2 0.50	X6X2 0.54	X4X1 0.68	X6X3 0.72
	X9X2 0.65	X9X2 0.64	X2X1 0.49	X2X1 0.51	X4X2 0.64	X6X5 0.70
	X6X2 0.60	X6X2 0.59	X9X4 0.47	X5X2 0.49	X6X3 0.64	X9X6 0.67
	X2X1 0.59	X2X1 0.57	X9X5 0.45	X4X2 0.49	X6X4 0.64	X5X4 0.63

References

1. Qi, G.; Miao, Y.; Xie, F.; Teng, C.; Wang, C.; Wang, Z. Synergistic Evolution of $PM_{2.5}$ and O_3 Concentrations: Evidence from Environmental Kuznets Curve Tests in the Yellow River Basin. *Sustainability* **2024**, *16*, 4744. [CrossRef]
2. *GB 3095-2012*; Ambient Air Quality Standards. China Environmental Science Press: Beijing, China, 2012.
3. He, J.; Yang, K.; Li, X.; Tang, W.; Shao, C.; Jiang, Y.; Ding, B. China Meteorological Forcing Dataset v2.0 (1951–2020). National Tibetan Plateau/Third Pole Environment Data Center. 2024. Available online: https://cstr.cn/18406.11.Atmos.tpdc.302088 (accessed on 23 February 2026).
4. Li, Q.; Chen, W.; Li, M.; Yu, Q.; Wang, Y. Identifying the Effects of Industrial Land Expansion on $PM_{2.5}$ Concentrations: A Spatiotemporal Analysis in China. *Ecol. Indic.* **2022**, *141*, 109069. [CrossRef]
5. Ma, Q.; Liu, Y.; Qiu, T.; Huang, T.; Deng, T.; Hu, Z.; Cui, T. Satellite-Observed Four-Dimensional Spatiotemporal Characteristics of Maritime Aerosol Types over the Coastal Waters of the Guangdong–Hong Kong–Macao Greater Bay Area and the Northern South China Sea. *Remote Sens.* **2022**, *14*, 5464. [CrossRef]
6. Xiong, L.; De Jong, M.; Wang, F.; Cheng, B.; Yu, C. Spatial Spillover Effects of Environmental Pollution in China's Central Plains Urban Agglomeration. *Sustainability* **2018**, *10*, 994. [CrossRef]
7. Shu, Z.; Liu, Y.; Zhao, T.; Xia, J.; Wang, C.; Cao, L.; Wang, H.; Zhang, L.; Zheng, Y.; Shen, L.; et al. Elevated 3D Structures of $PM_{2.5}$ and Impact of Complex Terrain-Forcing Circulations on Heavy Haze Pollution over Sichuan Basin, China. *Atmos. Chem. Phys.* **2021**, *21*, 9253–9268. [CrossRef]
8. Xiong, J.; Bai, Y.; Zhao, T.; Zhou, Y.; Sun, X.; Xu, J.; Zhang, W.; Leng, L.; Xu, G. Synergistic Effect of Atmospheric Boundary Layer and Regional Transport on Aggravating Air Pollution in the Twain-Hu Basin: A Case Study. *Remote Sens.* **2022**, *14*, 5166. [CrossRef]
9. Kendrick, C.M.; Koonce, P.; George, L.A. Diurnal and Seasonal Variations of NO, NO_2 and $PM_{2.5}$ Mass as a Function of Traffic Volumes alongside an Urban Arterial. *Atmos. Environ.* **2015**, *122*, 133–141. [CrossRef]
10. Harrison, R.M.; Vu, T.V.; Jafar, H.; Shi, Z. More Mileage in Reducing Urban Air Pollution from Road Traffic. *Environ. Int.* **2021**, *149*, 106329. [CrossRef]
11. Kurtenbach, R.; Kleffmann, J.; Niedojadlo, A.; Wiesen, P. Primary NO_2 Emissions and Their Impact on Air Quality in Traffic Environments in Germany. *Environ. Sci. Eur.* **2012**, *24*, 21. [CrossRef]
12. Sicard, P.; Paoletti, E.; Agathokleous, E.; Araminienė, V.; Proietti, C.; Coulibaly, F.; De Marco, A. Ozone Weekend Effect in Cities: Deep Insights for Urban Air Pollution Control. *Environ. Res.* **2020**, *191*, 110193. [CrossRef]

13. Liu, J.; He, C.; Si, Y.; Li, B.; Wu, Q.; Ni, J.; Zhao, Y.; Hu, Q.; Du, S.; Lu, Z.; et al. Toward Better and Healthier Air Quality: Global $PM_{2.5}$ and O_3 Pollution Status and Risk Assessment Based on the New WHO Air Quality Guidelines for 2021. *Glob. Chall.* **2024**, *8*, 2300258. [CrossRef] [PubMed]
14. Zhou, Y.; Duan, W.; Chen, Y.; Yi, J.; Wang, B.; Di, Y.; He, C. Exposure Risk of Global Surface O_3 During the Boreal Spring Season. *Expo. Health* **2022**, *14*, 431–446. [CrossRef] [PubMed]
15. Gkatzelis, G.I.; Gilman, J.B.; Brown, S.S.; Eskes, H.; Gomes, A.R.; Lange, A.C.; McDonald, B.C.; Peischl, J.; Petzold, A.; Thompson, C.R.; et al. The Global Impacts of COVID-19 Lockdowns on Urban Air Pollution: A Critical Review and Recommendations. *Elem. Sci. Anthr.* **2021**, *9*, 00176. [CrossRef]
16. Roy, A.; Mandal, M.; Binha, S.K.; Prasad, D.; Popek, R.; Przybysz, A.; Sarkar, A. Festive Pollution: A Global Concern—A Comparative Study of Diwali in India and New Year's Eve in Poland. *Atmosphere* **2025**, *16*, 442. [CrossRef]
17. Roy, A.; Das, S.; Singh, P.; Mandal, M.; Kumar, M.; Rajlaxmi, A.; Vijayan, N.; Awasthi, A.; Chhetri, H.; Roy, S.; et al. Summer-Time Monitoring and Source Apportionment Study of Both Coarse, Fine, And Ultra-Fine Particulate Pollution In Eastern Himalayan Darjeeling: A Hint To Health Risk During Peak Tourist Season. *MAPAN* **2024**, *39*, 995–1009. [CrossRef]
18. Fleming, Z.L.; Doherty, R.M.; von Schneidemesser, E.; Malley, C.S.; Cooper, O.R.; Pinto, J.P.; Colette, A.; Xu, X.; Simpson, D.; Schultz, M.G.; et al. Tropospheric Ozone Assessment Report: Present-Day Ozone Distribution and Trends Relevant to Human Health. *Elem. Sci. Anthr.* **2018**, *6*, 12. [CrossRef]
19. Mohtar, A.A.A.; Latif, M.T.; Dominick, D.; Ooi, M.C.G.; Azhari, A.; Baharudin, N.H.; Hanif, N.M.; Chung, J.X.; Juneng, L. Spatiotemporal Variations of Particulate Matter and Their Association with Criteria Pollutants and Meteorology in Malaysia. *Aerosol Air Qual. Res.* **2022**, *22*, 220124. [CrossRef]
20. Bhatti, U.A.; Yan, Y.; Zhou, M.; Ali, S.; Hussain, A.; Huo, Q.; Yu, Z.; Yuan, L. Time Series Analysis and Forecasting of Air Pollution Particulate Matter ($PM_{2.5}$): An SARIMA and Factor Analysis Approach. *IEEE Access* **2021**, *9*, 41019–41031. [CrossRef]
21. Michalski, G.; Bhattacharya, S.K.; Girsch, G. NO_x Cycle and the Tropospheric Ozone Isotope Anomaly: An Experimental Investigation. *Atmos. Chem. Phys.* **2014**, *14*, 4935–4953. [CrossRef]
22. Hu, Q.; Ji, X.; Hong, Q.; Li, J.; Li, Q.; Ou, J.; Liu, H.; Xing, C.; Tan, W.; Chen, J.; et al. Vertical Evolution of Ozone Formation Sensitivity Based on Synchronous Vertical Observations of Ozone and Proxies for Its Precursors: Implications for Ozone Pollution Prevention Strategies. *Environ. Sci. Technol.* **2024**, *58*, 4291–4301. [CrossRef]
23. Li, X.; Zhang, R.; Tripathee, L.; Yu, F.; Guo, J.; Yang, W.; Guo, J.; Kang, S.; Cao, J. Characteristics, Sources, and Health Risk Assessment of Atmospheric Particulate Mercury in Guanzhong Basin. *Environ. Pollut.* **2024**, *342*, 123071. [CrossRef] [PubMed]
24. Wang, D.; Li, X.; Duan, X.; Yang, H.; Zhang, B. Exploring the Spatiotemporal Patterns of County-Scale $PM_{2.5}$ Drivers in Shandong Province from 2000 to 2020. *PLoS ONE* **2024**, *19*, e0310190. [CrossRef] [PubMed]
25. Wang, X.; Yang, C.; Cui, J.; Wan, Z.; Xue, Y.; Guo, Q.; Sun, H.; Tian, Y.; Chen, D.; Zhao, W.; et al. Spatial and Temporal Differentiation and Its Driving Factors of Air Quality in the Economic Circle of Shandong Province during 2013–2020. *Ecotoxicol. Environ. Saf.* **2024**, *284*, 116934. [CrossRef] [PubMed]
26. Zhang, X.; Lin, Y.; Cheng, C.; Li, J. Determinant Powers of Socioeconomic Factors and Their Interactive Impacts on Particulate Matter Pollution in North China. *Int. J. Environ. Res. Public Health* **2021**, *18*, 6261. [CrossRef]
27. Wang, L.; Chen, B.; Ouyang, J.; Mu, Y.; Zhen, L.; Yang, L.; Xu, W.; Tang, L. Causal-Inference Machine Learning Reveals the Drivers of China's 2022 Ozone Rebound. *Environ. Sci. Ecotechnol.* **2025**, *24*, 100524. [CrossRef]
28. Liu, X.; Zhao, C.; Niu, J.; Su, F.; Yao, D.; Xu, F.; Yan, J.; Shen, X.; Jin, T. Spatiotemporal Patterns and Regional Transport of Ground-Level Ozone in Major Urban Agglomerations in China. *Atmosphere* **2022**, *13*, 301. [CrossRef]
29. Ding, Y.; Zhang, M.; Qian, X.; Li, C.; Chen, S.; Wang, W. Using the Geographical Detector Technique to Explore the Impact of Socioeconomic Factors on $PM_{2.5}$ Concentrations in China. *J. Clean. Prod.* **2019**, *211*, 1480–1490. [CrossRef]
30. Qiao, P.; Yang, S.; Lei, M.; Chen, T.; Dong, N. Quantitative Analysis of the Factors Influencing Spatial Distribution of Soil Heavy Metals Based on Geographical Detector. *Sci. Total Environ.* **2019**, *664*, 392–413. [CrossRef]
31. Bai, L.; Jiang, L.; Yang, D.; Liu, Y. Quantifying the Spatial Heterogeneity Influences of Natural and Socioeconomic Factors and Their Interactions on Air Pollution Using the Geographical Detector Method: A Case Study of the Yangtze River Economic Belt, China. *J. Clean. Prod.* **2019**, *232*, 692–704. [CrossRef]
32. Yun, G.; Zuo, S.; Dai, S.; Song, X.; Xu, C.; Liao, Y.; Zhao, P.; Chang, W.; Chen, Q.; Li, Y.; et al. Individual and Interactive Influences of Anthropogenic and Ecological Factors on Forest $PM_{2.5}$ Concentrations at an Urban Scale. *Remote Sens.* **2018**, *10*, 521. [CrossRef]
33. Yu, M.-Y.; Xu, Y.; Li, J.-Q.; Lu, X.-C.; Xing, H.-Q.; Ma, M.-L. Geographic Detector-Based Spatiotemporal Variation and Influence Factors Analysis of $PM_{2.5}$ in Shandong, China. *Pol. J. Environ. Stud.* **2021**, *30*, 463–475. [CrossRef]
34. Barnes, P.W.; Williamson, C.E.; Lucas, R.M.; Robinson, S.A.; Madronich, S.; Paul, N.D.; Bornman, J.F.; Bais, A.F.; Sulzberger, B.; Wilson, S.R.; et al. Ozone Depletion, Ultraviolet Radiation, Climate Change and Prospects for a Sustainable Future. *Nat. Sustain.* **2019**, *2*, 569–579. [CrossRef]
35. Bais, A.F.; Bernhard, G.; McKenzie, R.L.; Aucamp, P.J.; Young, P.J.; Ilyas, M.; Jöckel, P.; Deushi, M. Ozone—Climate Interactions and Effects on Solar Ultraviolet Radiation. *Photochem. Photobiol. Sci.* **2019**, *18*, 602–640. [CrossRef] [PubMed]

36. Cao, T.; Wang, H.; Chen, X.; Li, L.; Lu, X.; Lu, K.; Fan, S. Rapid Increase in Spring Ozone in the Pearl River Delta, China during 2013–2022. *NPJ Clim. Atmos. Sci.* **2024**, *7*, 309. [CrossRef]
37. Bernhard, G.H.; Bais, A.F.; Aucamp, P.J.; Klekociuk, A.R.; Liley, J.B.; McKenzie, R.L. Stratospheric Ozone, UV Radiation, and Climate Interactions. *Photochem. Photobiol. Sci.* **2023**, *22*, 937–989. [CrossRef]
38. Li, Z.; Bi, J.; Liu, Y.; Hu, X. Forecasting O_3 and NO_2 Concentrations with Spatiotemporally Continuous Coverage in Southeastern China Using a Machine Learning Approach. *Environ. Int.* **2025**, *195*, 109249. [CrossRef]
39. Zhang, X.; Yan, B.; Du, C.; Cheng, C.; Zhao, H. Quantifying the Interactive Effects of Meteorological, Socioeconomic, and Pollutant Factors on Summertime Ozone Pollution in China during the Implementation of Two Important Policies. *Atmos. Pollut. Res.* **2021**, *12*, 101248. [CrossRef]
40. He, Y.; Li, L.; Wang, H.; Xu, X.; Li, Y.; Fan, S. A Cold Front Induced Co-Occurrence of O_3 and $PM_{2.5}$ Pollution in a Pearl River Delta City: Temporal Variation, Vertical Structure, and Mechanism. *Environ. Pollut.* **2022**, *306*, 119464. [CrossRef]
41. Liu, H.; Lei, J.; Liu, Y.; Zhu, T.; Chan, K.; Chen, X.; Wei, J.; Deng, F.; Li, G.; Jiang, Y.; et al. Hospital Admissions Attributable to Reduced Air Pollution Due to Clean-Air Policies in China. *Nat. Med.* **2025**, *31*, 1688–1697. [CrossRef]
42. Hidy, G.M. An Historical Experiment: Los Angeles Smog Evolution Observed by Blimp. *J. Air Waste Manag. Assoc.* **2018**, *68*, 643–655. [CrossRef]
43. Bharadwaj, P.; Zivin, J.G.; Mullins, J.T.; Neidell, M. Early-Life Exposure to the Great Smog of 1952 and the Development of Asthma. *Am. J. Respir. Crit. Care Med.* **2016**, *194*, 1475–1482. [CrossRef]
44. Pathak, M.; Kuttippurath, J. Elucidating the Changing Particulate Matter Pollution and Associated Health Effects in Rural India during 2000–2019. *Environ. Pollut.* **2024**, *348*, 123830. [CrossRef] [PubMed]
45. Requia, W.J.; Vicedo-Cabrera, A.M.; Amini, H.; da Silva, G.L.; Schwartz, J.D.; Koutrakis, P. Short-Term Air Pollution Exposure and Hospital Admissions for Cardiorespiratory Diseases in Brazil: A Nationwide Time-Series Study between 2008 and 2018. *Environ. Res.* **2023**, *217*, 114794. [CrossRef] [PubMed]
46. Rudke, A.P.; Martins, L.D.; Martins, J.A.; Mantoani, M.C.; Andrade, M.d.F.; Kumar, P.; Alves, R.A.; Pedruzzi, R.; Thompson, T.; Sobrinho, O.M.; et al. Where There Is Smoke, There Is Fire: Long- and Mid-Range Biomass Burning Role on Sao Paulo's State Air Quality. *Environ. Pollut.* **2025**, *384*, 126993. [CrossRef] [PubMed]
47. Liu, S.; Geng, G.; Xiao, Q.; Zheng, Y.; Liu, X.; Cheng, J.; Zhang, Q. Tracking Daily Concentrations of $PM_{2.5}$ Chemical Composition in China since 2000. *Environ. Sci. Technol.* **2022**, *56*, 16517–16527. [CrossRef]
48. Jin, Y.; Andersson, H.; Zhang, S. Air Pollution Control Policies in China: A Retrospective and Prospects. *Int. J. Environ. Res. Public Health* **2016**, *13*, 1219. [CrossRef]
49. Song, C.; Wu, L.; Xie, Y.; He, J.; Chen, X.; Wang, T.; Lin, Y.; Jin, T.; Wang, A.; Liu, Y.; et al. Air Pollution in China: Status and Spatiotemporal Variations. *Environ. Pollut.* **2017**, *227*, 334–347. [CrossRef]
50. Wan, K.; Shackley, S.; Doherty, R.M.; Shi, Z.; Zhang, P.; Golding, N. Science-Policy Interplay on Air Pollution Governance in China. *Environ. Sci. Policy* **2020**, *107*, 150–157. [CrossRef]
51. Kelly, F.J.; Fuller, G.W.; Walton, H.A.; Fussell, J.C. Monitoring Air Pollution: Use of Early Warning Systems for Public Health. *Respirology* **2012**, *17*, 7–19. [CrossRef]
52. Su, L.; Gao, C.; Ren, X.; Zhang, F.; Cao, S.; Zhang, S.; Chen, T.; Liu, M.; Ni, B.; Liu, M. Understanding the Spatial Representativeness of Air Quality Monitoring Network and Its Application to $PM_{2.5}$ in the Mainland China. *Geosci. Front.* **2022**, *13*, 101370. [CrossRef]
53. Wei, J.; Li, Z.; Lyapustin, A.; Wang, J.; Dubovik, O.; Schwartz, J.; Sun, L.; Li, C.; Liu, S.; Zhu, T. First Close Insight into Global Daily Gapless 1 Km $PM_{2.5}$ Pollution, Variability, and Health Impact. *Nat. Commun.* **2023**, *14*, 8349. [CrossRef]
54. Bi, J.; Knowland, K.E.; Keller, C.A.; Liu, Y. Combining Machine Learning and Numerical Simulation for High-Resolution $PM_{2.5}$ Concentration Forecast. *Environ. Sci. Technol.* **2022**, *56*, 1544–1556. [CrossRef] [PubMed]
55. Kong, L.; Tang, X.; Zhu, J.; Wang, Z.; Li, J.; Wu, H.; Wu, Q.; Chen, H.; Zhu, L.; Wang, W.; et al. A 6-Year-Long (2013–2018) High-Resolution Air Quality Reanalysis Dataset in China Based on the Assimilation of Surface Observations from CNEMC. *Earth Syst. Sci. Data* **2021**, *13*, 529–570. [CrossRef]
56. Bai, K.; Li, K.; Wu, C.; Chang, N.-B.; Guo, J. A Homogenized Daily in Situ $PM_{2.5}$ Concentration Dataset from the National Air Quality Monitoring Network in China. *Earth Syst. Sci. Data* **2020**, *12*, 3067–3080. [CrossRef]
57. Lu, S.; Gong, S.; He, J. Uncertainty Analysis of Spatiotemporal Characteristics of Haze Pollution from 1961 to 2017 in China. *Atmos. Pollut. Res.* **2020**, *11*, 310–318. [CrossRef]
58. Liu, Y.; Adamu, A.T.; Tan, J. Spatial Characterization of Periodic Behaviors of Ground $PM_{2.5}$ Concentration across the Yangtze River Delta and the North China Plain during 2014–2024: A New Insight on Driving Processes of Regional Air Pollution. *Environ. Res.* **2025**, *277*, 121648. [CrossRef]
59. Yu, B.; Huang, C.; Liu, Z.; Wang, H.; Wang, L. A Chaotic Analysis on Air Pollution Index Change over Past 10 Years in Lanzhou, Northwest China. *Stoch. Environ. Res. Risk Assess.* **2011**, *25*, 643–653. [CrossRef]

60. Jiang, Z.; Jolleys, M.D.; Fu, T.-M.; Palmer, P.; Ma, Y.; Tian, H.; Li, J.; Yang, X. Spatiotemporal and Probability Variations of Surface $PM_{2.5}$ over China between 2013 and 2019 and the Associated Changes in Health Risks: An Integrative Observation and Model Analysis. *Sci. Total Environ.* **2020**, *723*, 137896. [CrossRef]
61. Li, S.; Zou, B.; Liu, N.; Xue, C.; Li, S.; Wang, Y.; Xu, Y. Proactive Synergistic Control of $PM_{2.5}$ and Ozone through Urban Planning: Longitudinal Data Analysis of 274 Chinese Cities from 2005 to 2020. *Geo-Spat. Inf. Sci.* **2025**, *28*, 3133–3151. [CrossRef]
62. Jiang, F.; Chen, B.; Li, P.; Jiang, J.; Zhang, Q.; Wang, J.; Deng, J. Spatio-Temporal Evolution and Influencing Factors of Synergizing the Reduction of Pollution and Carbon Emissions-Utilizing Multi-Source Remote Sensing Data and GTWR Model. *Environ. Res.* **2023**, *229*, 115775. [CrossRef]
63. Liu, L.; Liu, Y.; Cheng, F.; Yu, Y.; Wang, J.; Wang, C.; Nong, L.; Deng, H. Remote Sensing Estimation of Regional $PM_{2.5}$ Based on GTWR Model-A Case Study of Southwest China. *Environ. Pollut.* **2024**, *351*, 124057. [CrossRef] [PubMed]
64. Yang, L.; Qin, C.; Li, K.; Deng, C.; Liu, Y. Quantifying the Spatiotemporal Heterogeneity of $PM_{2.5}$ Pollution and Its Determinants in 273 Cities in China. *Int. J. Environ. Res. Public Health* **2023**, *20*, 1183. [CrossRef] [PubMed]
65. Mun, H.; Li, M.; Jung, J. Spatial-Temporal Characteristics and Influencing Factors of Particulate Matter: Geodetector Approach. *Land* **2022**, *11*, 2336. [CrossRef]
66. Chen, Y.; Li, H.; Karimian, H.; Li, M.; Fan, Q.; Xu, Z. Spatio-Temporal Variation of Ozone Pollution Risk and Its Influencing Factors in China Based on Geodetector and Geospatial Models. *Chemosphere* **2022**, *302*, 134843. [CrossRef]
67. Shi, T.; Peng, Y.; Ma, X.; Han, G.; Zhang, H.; Pei, Z.; Li, S.; Mao, H.; Zhang, X.; Gong, W. China's "Coal-to-Gas" Policy Had Large Impact on PM1.0 Distribution during 2016–2019. *J. Environ. Manag.* **2024**, *359*, 121071. [CrossRef]
68. Dilawar, A.; Chen, B.; Ul-Haq, Z.; Amir, M.; Arshad, A.; Hassan, M.; Guo, M.; Shafeeque, M.; Fang, J.; Song, B.; et al. Investigating the Potential Climatic Effects of Atmospheric Pollution across China under the National Clean Air Action Plan. *Remote Sens.* **2023**, *15*, 2084. [CrossRef]
69. Zhang, K.; de Leeuw, G.; Yang, Z.; Chen, X.; Jiao, J. The Impacts of the COVID-19 Lockdown on Air Quality in the Guanzhong Basin, China. *Remote Sens.* **2020**, *12*, 3042. [CrossRef]
70. Khan, N.; Hashim, B.M.; Sa'adi, Z.; Kemarau, R.A.; Goliatt, L.; Abdulameer, S.F.; Yaseen, Z.M.; Shahid, S. A Novel Index for Assessing the Compound Drought, Heat Waves, and Air Pollution Extremes. *Urban Clim.* **2026**, *65*, 102726. [CrossRef]
71. Li, M.; Huang, X.; Yan, D.; Lai, S.; Zhang, Z.; Zhu, L.; Lu, Y.; Jiang, X.; Wang, N.; Wang, T.; et al. Coping with the Concurrent Heatwaves and Ozone Extremes in China under a Warming Climate. *Sci. Bull.* **2024**, *69*, 2938–2947. [CrossRef]
72. Jinping, L.; Mingzhe, L.; Tie, L.; Yanqun, R.; Qingfeng, H.; Shalamzari, M.J.; Pham, Q.B.; Peipei, H. Comprehensive Analysis of Compound Drought and Heatwave Events in China over Recent Decades Based on Regional Event Identification Algorithm. *Int. J. Digit. Earth* **2025**, *18*, 2514709. [CrossRef]
73. Liu, J.; Li, M.; Pham, Q.B.; Liu, T.; Ren, Y.; Shalamzari, M.J.; He, P. From Historical to Future Scenarios: A Deep Learning and Dynamical Detection Framework for Compound Drought and Heatwave Events. *Expert Syst. Appl.* **2026**, *307*, 131105. [CrossRef]
74. Geng, G.; Zheng, Y.; Zhang, Q.; Xue, T.; Zhao, H.; Tong, D.; Zheng, B.; Li, M.; Liu, F.; Hong, C.; et al. Drivers of $PM_{2.5}$ Air Pollution Deaths in China 2002–2017. *Nat. Geosci.* **2021**, *14*, 645–650. [CrossRef]
75. Han, J.; Li, Y.; Li, F. Spatio-Temporal Distribution Characteristic of $PM_{2.5}$ Concentration and the Difference of $PM_{2.5}$ Concentration between Urban Areas and Rural Areas in China from 2000 to 2015. *Acta Ecol. Sin.* **2019**, *39*, 2954–2962. [CrossRef]
76. Hua, C.; Zhang, Z.; Miao, J.; Han, J.; Zhu, Z. Spatial Coordination and Industrial Pollution of Urban Agglomerations: Evidence from the Yellow River Basin in China. *Expert Syst.* **2025**, *42*, e13548. [CrossRef]
77. Zhang, Z.; Wang, S.; Zhang, J. Spatiotemporal Evolution of Carbon Budget and Carbon Compensation Zoning of Urban Agglomerations in the Yellow River Basin. *Sci. Rep.* **2024**, *14*, 17984. [CrossRef]
78. Su, Z.; Yang, Y.; Wang, Y.; Zhang, P.; Luo, X. Study on Spatiotemporal Evolution Features and Affecting Factors of Collaborative Governance of Pollution Reduction and Carbon Abatement in Urban Agglomerations of the Yellow River Basin. *Int. J. Environ. Res. Public Health* **2023**, *20*, 3994. [CrossRef] [PubMed]
79. Han, L.; Han, M.; Wang, Y.; Wang, H.; Niu, J. Spatial and Temporal Characteristic of $PM_{2.5}$ and Influence Factors in the Yellow River Basin. *Front. Public Health* **2024**, *12*, 1403414. [CrossRef]

Disclaimer/Publisher's Note: The statements, opinions and data contained in all publications are solely those of the individual author(s) and contributor(s) and not of MDPI and/or the editor(s). MDPI and/or the editor(s) disclaim responsibility for any injury to people or property resulting from any ideas, methods, instructions or products referred to in the content.